Implementation and validation of a bonded particle model to predict rheological properties of viscoelastic materials

Michael Mascara [a,b], Arno Mayrhofer [b], Stefan Radl [a,*], Christoph Kloss [b]

[a] *Institute of Process and Particle Engineering, Graz University of Technology, Inffeldgasse 13, Graz, 8010, Austria*
[b] *DCS Computing GmbH, Industriezeile 35, Linz, 4020, Austria*

ABSTRACT

This work focuses on implementing a particle-based method able to characterize viscoelastic materials whose rheological properties, such as storage modulus G' and loss modulus G'', are known. It is based on the bonded particle model, with the elastic constitutive relation here substituted with a viscoelastic one to capture time-scale effects. The Burgers model, vastly used in literature to model viscoelastic systems, is discretized and implemented. The test case used for calibration comprises of a cubic lattice, sheared with a periodic motion, to mimic the effect of a shear rheometer. After appropriate filtering of the stress response, the rheological properties are obtained, highlighting the effect of the lattice geometry, as well as the particle size, on the accuracy of the model. Moreover, the Burgers parameters are calibrated by analytically fitting the experimental dataset, showing the limitation of the Burgers model. The micro-contact parameters are obtained from the macro parameters through appropriate scaling. After completing a frequency sweep, the simulated G' and G'' show a relatively large error, around 25% for G' for example. For this reason, a more robust model, namely the generalized Maxwell model, has been implemented. The calibration procedure is performed in the same fashion as for the Burgers model. Moreover, the tangential micro-contact parameters are scaled w.r.t. the normal ones. This scaling parameter, called α, is calibrated by minimizing the root mean square error between simulation and experimental data, giving errors below 10% in both G' and G'' for a large dataset. Additionally, a full ring plate-plate rheometer setup is simulated, and the simulation is compared with the given experimental dataset, again finding a good agreement.

1. Introduction

One of the first attempts at describing viscoelasticity was done by Giesekus (Giesekus, 1982). In his mostly analytical work, he modified the stress tensor definition in the momentum equation of a fluid by considering additional linear and non-linear stress-strain constitutive relations, with tensors and parameters describing the network of a given material. Given the complexity of his formulation, an analytical solution was obtained for simple flows. With the advent of numerical methods, it has been possible to push the frontier of solving complex flows involving viscoelastic materials. Still, it simultaneously introduces all the challenges these methods may add. One degree of complexity is modeling the interface between the material and a solid surface (Favero et al., 2010), where a fine mesh size is needed to capture near-wall flows. Additionally, multi-mode analysis is needed in complex geometries to achieve a reasonable agreement with experimental data (Tsai & Miller, 2014). The finite element method has also been used to predict the properties of viscoelastic materials (Bottoni et al., 2007; Katouzian et al., 2021), with the limitation of being unable to deal with flowing scenarios. Hence, it is hard for this method to describe the material's behavior in an industrial application involving strong viscous effects, usually encountered with dynamically moving boundary conditions and extreme situations. At the same time, since Cundall and Strack developed the first discrete element method code (Cundall & Strack, 1979), a whole new approach was now possible, where the absence of a volumetric mesh would greatly simplify the simulations.

* Corresponding author.
E-mail addresses: michael.mascara@dcs-computing.com (M. Mascara), radl@tugraz.at (S. Radl).

On the one hand, mesh-based methods are handy when describing single-phase materials. On the other hand, particle-based methods can describe heterogeneous systems with the presence of polydisperse phases (Zubov et al., 2019), multi-phase conglomerates, such as oil sand (Gbadam & Frimpong, 2017), coke-pitch mixtures (Majidi et al., 2016), and asphalt (Dondi et al., 2013), to cite some. Most of the work involving numerical modeling and simulations done in literature is material specific (Cao, 2020; Mohammed et al., 2013), i.e. it has been designed and tuned for a particular application and/or material. The idea of this work is the extension of a particle-based method to both homogeneous and inhomogeneous systems. It can predict the rheological properties of a large variety of materials equally, which can then be used to optimize a certain industrial process involving said materials. A particle-based method is described, tested, and validated against experimental data to achieve this. It is based on the bonded particle model (BPM), first introduced by Potyondy and Cundall (Potyondy & Cundall, 2004) where particles would interact with each other at contact through an elastic beam, to describe the amorphous properties of rocks, defined as a heterogeneous system of irregularly shaped or spherical particles. The idea is to extend this model to viscoelastic materials by substituting the purely elastic relations used in the original BPM definition with a viscoelastic interaction. In this case, the Burgers model is initially implemented in the commercial software Aspherix®, showing the discretization scheme for the constitutive relation. Moreover, a test calibration is performed using an existing dataset, which shows that another method is needed to improve accuracy, namely the generalized Maxwell model.

The idea behind the realization of this article is the creation of a unique particle-based method capable of predicting the flow of fluids and granular media whose rheological properties are known. This would then serve as an initial step to calibrating this model and tuning it so it can be used in various industrial processes dealing with viscoelastic materials without using complex mesh-based methods.

2. Methodology

Introducing a bond between particles opens a new door to the modeling of cohesive powders and suspensions with cohesive particles, e.g., cement. Unlike cohesive models, the BPM is not bound to purely granular materials. Still, it can be extended to various systems, where, even though two or more phases can be distinguished at a microscopic level, they are macroscopically homogeneous. Moreover, the particles do not need to be in contact to exchange forces. To achieve this, the particles radii are multiplied by a constant parameter, called the radius multiplier λ, and the overlap between the increased radii is computed. Starting, for simplicity, with two particles with equal radii r, positions $\overrightarrow{x}_i$ $\overrightarrow{x}_j$, as shown in Fig. 1, a bond is formed when the distance between the particles d is less or equal than the sum of the increased radii, or $d = |\overrightarrow{x}_i - \overrightarrow{x}_j| \leq 2\lambda r$. In general, the length and radius of the bond are defined at its creation to be, respectively, $L = d$ and $R = \lambda \min(r_i, r_j)$ in the case of particles with different sizes. The value of the radius multiplier is usually chosen according to the distance between neighboring particles in such a way to ensure the bond formation. For example, if two particles are distant 2 mm and their radii are 0.4 mm, if one would like for these particles to be bonded, a value of $\lambda > 1.25$ is needed to ensure overlap.

2.1. Modified BPM with Burgers relation

As mentioned, the purely elastic constitutive relation used in the original BPM formulation (Potyondy & Cundall, 2004) is here
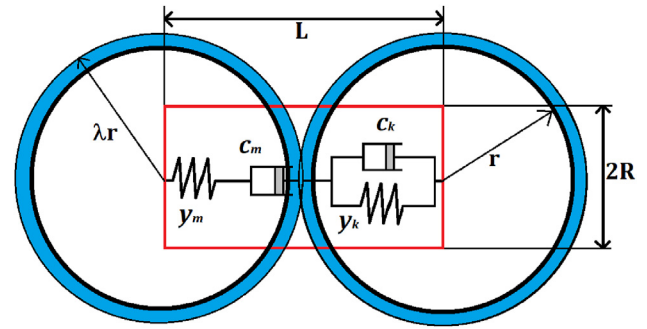

Fig. 1. Schematic of the bonded particle model with Burgers representation for the normal direction. An equivalent representation is used for the shear direction (visualization omitted for simplicity).

substituted with a viscoelastic relation. Even though the original formulation of the BPM could handle viscoelasticity, since it also has a damping element in its implementation, some drawbacks must be addressed. To begin with, the original BPM implementation can be described as a Kelvin−Voigt solid, the simplest viscoelastic model, consisting of a spring and a dashpot connected in parallel. Given the target of the model described in this article to be able to predict the behavior of a large range of materials, the Kelvin−Voigt model does not have enough timescales that would give generality to the original BPM. Moreover, calibration would be tricky because, to connect experimentally obtained rheological macro-properties with the model parameters, the analytical model response to the oscillatory shear test is needed, as it will be explained in more detail later. For this reason, it has been decided to start with at least two timescales, using a model already established as robust for a class of materials, namely the Burgers model, whose configuration is shown in Fig. 1. It is a combination of a Maxwell element, composed of a spring and a dashpot in series, connected in series with a Kelvin−Voigt element. The constitutive relation of Burgers materials has the following equation

$$\tau_k \tau_m \frac{d^2\sigma}{dt^2} + \left[\tau_k + \tau_m + \frac{\mu_k}{k_m}\right] \frac{d\sigma}{dt} + \sigma = \tau_k \mu_m \frac{d^2\varepsilon}{dt} + \mu_m \frac{d\varepsilon}{dt}, \tag{1}$$

where, $\tau_m = \mu_m/k_m$ and $\tau_k = \mu_k/k_k$ are the Kelvin and Maxwell time, respectively, computed from the spring constant k and the dashpot constant μ. Furthermore, σ is the stress acting on the element, and ε is the strain. Eq. (1) can be converted in its respective force-displacement formulation, as it is easier to handle for the implementation in the DEM code, resulting in

$$\tau_k \tau_m \frac{d^2f}{dt^2} + \left[\tau_k + \tau_m + \frac{c_k}{y_m}\right] \frac{df}{dt} + f = \tau_k c_m \frac{d^2u}{dt} + c_m \frac{du}{dt}, \tag{2}$$

where, $f = \sigma/A_b$ is the force acting on the element, $A_b = \pi R^2$ is the bond cross-section area, u is the displacement of the element, and c_m, c_k, y_m, y_k are the micro-contact parameters, which are computed from the macro-parameters as (Potyondy & Cundall, 2004):

$$c_m = \frac{A_b}{L}\mu_m, \ c_k = \frac{A_b}{L}\mu_k, \ y_m = \frac{A_b}{L}k_m, \ y_k = \frac{A_b}{L}k_k, \tag{3}$$

where, L is the bond length defined at the section's beginning.

2.1.1. Discretization of the Burgers equation

Given certain initial conditions, the simulation can be carried out if we can close the simulation loop, making it possible to solve the system dynamics. To achieve this, we need to compute

first the forces acting on the particles through the constitutive relation, then use the newly computed forces to integrate the equation of motion of each particle. To begin with, the visco-elastic constitutive relation is discretized numerically, which computes the forces acting between bonded particles as a function of the relative motion. The initial distribution of the particles acts as a boundary condition. In contrast, at the first timestep, initial conditions dictate the motion of all or some of the particles in the system. The displacement and displacement rate in the relative motion between particles are the independent variables in the discretized constitutive relations, which calculate the new forces. Ultimately, the new forces are used to numerically integrate the equation of motion to obtain new displacements, closing the computational loop. For the interested reader, please refer to the code for the calculation of Hertzian and bond forces in the Appendix to have more insights on the working principles of the numerical scheme.

The following discretization is currently used in the commercial software Aspherix and PFC3D, described in Ref. (Gbadam, 2017). Starting from the Kelvin element and remembering that for elements in parallel, stresses are cumulative while displacements are equal, the following constitutive relation is found

$$f = y_k u_k + c_k \frac{du_k}{dt}, \tag{4}$$

which can be rewritten as a function of the displacement rate $\frac{du_k}{dt}$ of the Kelvin element and computed at timestep $n+\frac{1}{2}$, (please note that the superscripts in the following equations refer to the timestep at which the variables are computed and they are not exponents) leading to

$$\frac{du_k}{dt}\Big|_{n+\frac{1}{2}} = \frac{f^{\{n+\frac{1}{2}\}} - y_k u_k^{\{n+\frac{1}{2}\}}}{c_k}. \tag{5}$$

Applying a Taylor series expansion to the Kelvin element displacement, centered in $t = \Delta t(n+\frac{1}{2})$, with step width $\frac{\Delta t}{2}$, the following approximation for the first derivative is obtained

$$\frac{du_k}{dt}\Big|_{n+\frac{1}{2}} = \frac{u_k^{\{n+1\}} - u_k^{\{n\}}}{\Delta t} + \mathcal{O}(\Delta t^2). \tag{6}$$

Substituting Eq. (6) into Eq. (5), taking average values for the other variables and re-arranging the terms to obtain an equation as a function of the new timestep displacement, leads to the following

$$u_k^{\{n+1\}} = \frac{1}{2\tau_k + \Delta t}\left[\frac{\Delta t}{y_k}(f^{\{n+1\}} + f^{\{n\}}) + u_k^{\{n\}}(2\tau_k - \Delta t)\right]. \tag{7}$$

For the Maxwell element, the constitutive relation is obtained by considering that the stress/force seen by each element in series is equal while the deformation/displacement is different, giving

$$\frac{du_m}{dt} = \frac{1}{y_m}\frac{df}{dt} + \frac{f}{c_m}. \tag{8}$$

Similarly, as it has been done for the Kelvin element, the same discretization scheme can be applied to the displacement rate of the Maxwell element, with the difference that now the derivative of the force appears. Once the scheme is applied, it is possible to re-arrange the terms to obtain

$$u_m^{\{n+1\}} = \frac{f^{\{n+1\}} - f^{\{n\}}}{y_m} + \Delta t\frac{f^{\{n+1\}} + f^{\{n\}}}{2c_m} + u_m^{\{n\}}. \tag{9}$$

Finally, knowing that $u = u_k + u_m$, deriving it once w.r.t. time and applying a central difference scheme as done in Eq. (6), the new timestep force value can be computed from the old timestep forces and displacements as

$$f^{\{n+1\}} = \frac{u^{\{n+1\}} - u^{\{n\}} + \frac{2\Delta t}{2\tau_k + \Delta t}u_k^{\{n\}} - Af^{\{n\}}}{B}, \tag{10}$$

where $A = \frac{\Delta t}{2c_k + \Delta t} + \frac{1}{y_m} + \frac{\Delta t}{2c_m}$ and $B = \frac{\Delta t}{2c_k + \Delta t} - \frac{1}{y_m} + \frac{\Delta t}{2c_m}$.

Furthermore, the displacements in normal and shear directions are defined from the relative motion between the particles, which is solved at each timestep by numerically integrating Newton's second law. Eq. (10) is scalar, but the old force and kelvin displacement values for each direction are stored as vectors. To be able to substitute them in the discretization, a semi-projection is first carried out (it is shown for the normal direction, but exactly the same procedure stands for the shear direction)

$$\begin{aligned} f_{norm}^{\{n\}} &= \overrightarrow{f}_{norm}^{\{n\}} \cdot \hat{n}^{\{n+1\}} \\ u_{k,norm}^{\{n\}} &= \overrightarrow{u}_{k,norm}^{\{n\}} \cdot \hat{n}^{\{n+1\}}, \end{aligned} \tag{11a}$$

where, $\hat{n}^{\{n+1\}}$ is the unit vector in the relative normal direction between the particles in contact. Once the new timestep force, as well as the kelvin displacement, are computed, they are projected onto the new normal direction

$$\begin{aligned} \overrightarrow{f}_{norm}^{\{n+1\}} &= f_{norm}^{\{n+1\}} \cdot \hat{n}^{\{n+1\}} \\ \overrightarrow{u}_{k,norm}^{\{n+1\}} &= u_{k,norm}^{\{n+1\}} \cdot \hat{n}^{\{n+1\}}. \end{aligned} \tag{11b}$$

2.2. The generalized Maxwell model

Together with the Burgers model, in this work, a generalized Maxwell model has been implemented due to the low accuracy of the former, which will be discussed later in this article. As the name suggests, the generalized Maxwell model is defined as a connection in parallel of a certain number of Maxwell elements, plus a spring and/or a dashpot, as depicted in Fig. 2. Even though it appears more complex than a Burgers model, its implementation is rather simple for two reasons. To begin with, the constitutive relation of Eq. (8) only contains the first derivatives in time, making it easier to discretize. Moreover, all elements undergo the same deformation, simplifying the implementation.

In the current work, a 4 element model is used, plus a spring. The choice of 4 elements comes from the fact that, when trying to fit experimental data on a large dataset, it has been observed that 3
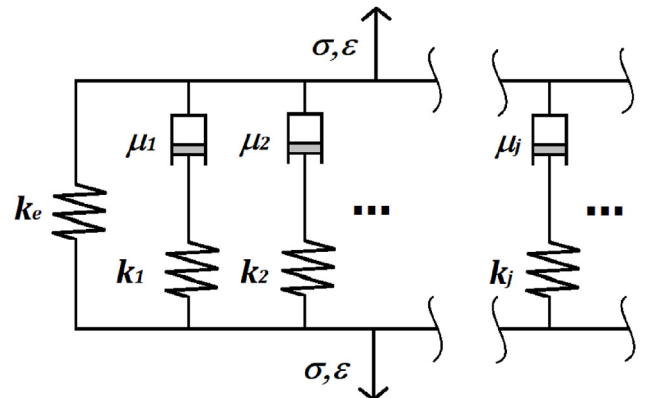

Fig. 2. Schematics of the generalized Maxwell model.

elements still lack accuracy, while 4 elements show a nice fit quality through the whole dataset, Figs. 15 and 16. A similar implementation has been used by Ren et al. (Ren & Sun, 2016), without bonds and in combination with different phases behaving elastically or viscoelatically depending on the nature of the contact. They obtained a relatively good agreement with experimental data. After scaling the macro-parameters into their respective micro-contact values as $y_j = k_j A_b / L$ and $c_j = \mu_j A_b / L$, the new timestep force relative to the single Maxwell element is computed from re-arranging Eq. (9) to give

$$f_j^{\{n+1\}} = \frac{u^{\{n+1\}} - u^{\{n\}} + f_j^{\{n\}}\left(\frac{1}{y_j} - \frac{\Delta t}{2c_j}\right)}{\frac{1}{y_j} + \frac{\Delta t}{2c_j}}.$$
(11c)

where the subscript j expresses the jth element in the model. Regarding the spring force f_{el}, a finite deformation approach is used, given that the relative positions at the bond creation are known. Hence, it is straightforward to compute the displacement relative to the bond creation timestep n_0, leading to $f_{el}^{\{n+1\}} = y_e(u^{\{n+1\}} - u^{\{n_0\}})$, with $y_e = k_e/A_b$, where k_e is the spring coefficient. The same applies to the shear direction as done in Sec. 2.2.1. Finally, the total force is just a sum of the single elements contribution, $f^{\{n+1\}} = \sum_j^4 f_j^{\{n+1\}} + f_{el}^{\{n+1\}}$.

2.2.1. Contact plane and displacements definition

In Eq. (10), the new timestep force is a function of the displacement $\Delta \vec{u}$, which is defined as the difference in relative distance between the particles at consecutive timesteps, $\Delta u = u^{\{n+1\}} - u^{\{n\}}$. After solving the particle's equation of motion, all the information on its position, velocity, and angular velocity are known at the timestep $n + 1$, while quantities at timestep n are saved. Let two particles i and j be in contact. Their relative displacement between two consecutive timesteps is $\Delta \vec{u} = \vec{r}^{\{n+1\}} - \vec{r}^{\{n\}}$, with $\vec{r} = \vec{x}_i - \vec{x}_j$ the relative position between the particles. While the definition of the unit normal vector is rather simple, being just the normalized $\vec{r}$, for the shear direction many different ways are possible, being there infinite orthogonal lines w.r.t. $\hat{n}$. The method adopted here is that of defining a contact plane between the timestep at which the bond is formed, called n_0, and the actual timestep and considering as shear direction the unit vector orthogonal to $\hat{n}$ which lays on said plane (Wang & Alonso-Marroquin, 2009). As a result, the unit shear vector is defined as

$$\hat{s}^{\{n+1\}} = \frac{\hat{n}^{\{n+1\}} \times (\hat{n}^{\{n+1\}} \times \hat{n}^{\{n_0\}})}{\left|\hat{n}^{\{n+1\}} \times (\hat{n}^{\{n+1\}} \times \hat{n}^{\{n_0\}})\right|}.$$
(12)

Once the principal directions at the new timestep contact are known, the semi-projected displacements in normal and shear directions are then computed similarly as done for the force and the kelvin displacement, giving

$$\Delta u_{norm} = \Delta \vec{u} \cdot \hat{n}^{\{n+1\}}$$

$$\Delta u_{shear} = \Delta \vec{u} \cdot \hat{s}^{\{n+1\}}.$$
(13a)

2.3. Simulation test case

The most common experimental setup to compute the rheological properties of viscoelastic materials is the Oscillatory Shear Rheometer. To mimic such experiments, in this study, an ordered lattice of particles is created, both in a simple cubic and in more

complex geometries, highlighting the differences. A lattice scaling is defined by a value $\delta = D(1 + \eta)$, where D is the diameter of the particles and η is a small and positive arbitrary number, which means all the particles are not overlapping. However, η is chosen according to the radius multiplier λ value so that bonds will form between neighboring particles. The faces of the cube are normal to the orthogonal global system of coordinates, and the boundary conditions are applied to the external layer of particles normal to the z-direction, as depicted in Fig. 3. The top layer of particles is maintained in the Small Amplitude Oscillatory Shear (SAOS) regime to ensure linearity, with a strain equal to 1%.

First, the stress response is computed as the sum of the forces f_i acting on the top layer of particles in the z-direction to measure the rheological properties, divided by the surface area defined by the aforementioned particles. Taking as an example the configuration of Fig. 3, the stress is computed as

$$\tau = \frac{\sum_i^{N^2} f_i}{(D + (N_{side} - 1) \cdot \delta)^2},$$
(13b)

where, $N_{side} = 6$ in this case.

It has been observed that for certain combinations of parameters and frequency applied, the eigenfrequency of the system would interfere with the stress signal, altering the output and eventually the quality of the results, Fig. 4. To solve this issue, a numerical fitting of the curve is needed, which is performed through a fast Fourier transform (FFT) analysis of the stress output, Fig. 5, and taking as amplitude the maximum of the FFT response and as frequency the one applied as a boundary condition, resulting in a nice fit for the stress, as observed in Fig. 4. Once the stress fit is complete, it is possible to compute the material's rheological properties through the complex modulus. As the name suggests, it is a complex number, defined as $G^* = G' + jG''$, where the real part G' is called storage modulus, the imaginary part G'' is the loss modulus, and j is the imaginary unit. They define the elastic and dissipative energy in the material, respectively. In a viscoelastic material, it is expected that given an input deformation of the form $\gamma(t) = \gamma_0 \sin(\omega t)$. The stress would have a response function of the form $\tau(t) = \tau_0 \sin(\omega t + \varphi)$ where φ is the phase lag between the two signals, Fig. 6, which in this case is computed by interpolating the stress response with a dummy function of the form $\tau_{int} = \tau_0 \sin(\omega t + c)$ and solving for c in a Python script. Once the interpolation returns a solution, all the information needed to characterize the material is available and the storage and loss moduli are computed respectively as $G' = \frac{\tau_0}{\gamma_0} \cos \varphi$ and $G'' = \frac{\tau_0}{\gamma_0} \sin \varphi$.
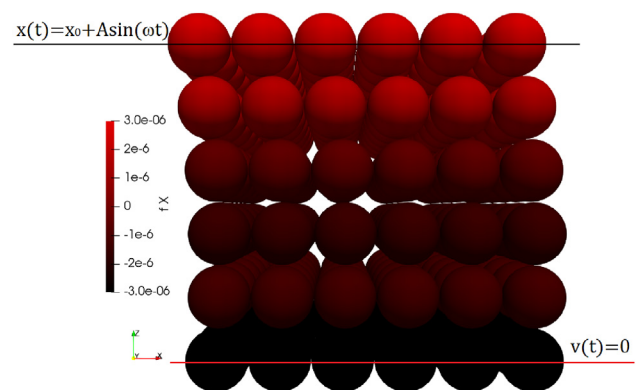

Fig. 3. Lattice geometry and boundary conditions. The top layer of particles is displaced with a periodic motion, governed by an amplitude of $A = 0.01(D + 5\delta)$ m and a frequency $\omega = 600$ rad/s, while the bottom layer is fixed. The coloring shows the x-component of the force on each particle expressed in Newton.
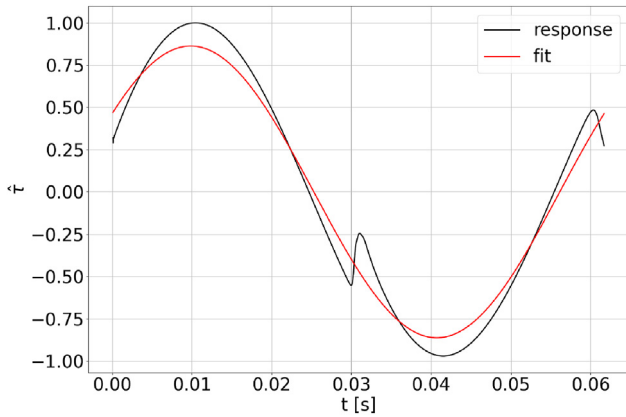
Fig. 4. Stress response obtained with oscillatory shear deformation, highlighting the eigenfrequency component disturbance and the fitted curve. The shear stress is normalized following $\hat{\tau} = \frac{\tau}{\max(\tau_r)}$, where τ_r is the material response stress signal.

2.3.1. Effect of particles size

It has already been anticipated that the model presented in this article aims to describe granular systems and homogeneous dispersion, which are usually granular or multiphase in the microscopic structure. DEM simulations do not need to refine their particle size to meet experimental data, as it would be done in a mesh-based method. Still, in our study, it has been observed that a decrease in particle size to simulate the same volume (hence with an increase in the number of particles per volume) would reflect a smaller error w.r.t. the analytical solution, as shown later in this article.

2.3.2. Accuracy of the Burgers model to predict elastic behavior

To have a known solution to compare the model to, the perfectly elastic behavior of a solid is used as an analytical comparison, with Young's modulus of $E_{el} = 1$ MPa. The parameters of the Burgers model needed to obtain an elastic behavior can be found from a simple order of magnitude analysis of the constitutive relation. Specifically, if one would divide Eq. (1) by $\mu_m \cdot \mu_k$ and let $\mu_m, \mu_k \rightarrow \infty$, the following is obtained

$$\frac{1}{k_m k_k} \frac{d^2\sigma}{dt^2} = \frac{1}{k_k} \frac{d^2\varepsilon}{dt^2}. \tag{14}$$
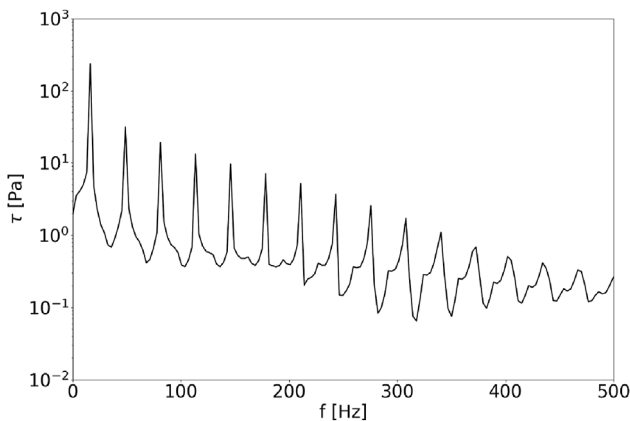

Fig. 5. Discrete Fast Fourier Transform of the stress signal output of an oscillatory shear rheometer simulation. The FFT analysis is performed using a Python script. Note that the presence of numerous eigenfrequencies, in addition to the frequency of oscillation, is recognizable via the multiple local maxima.
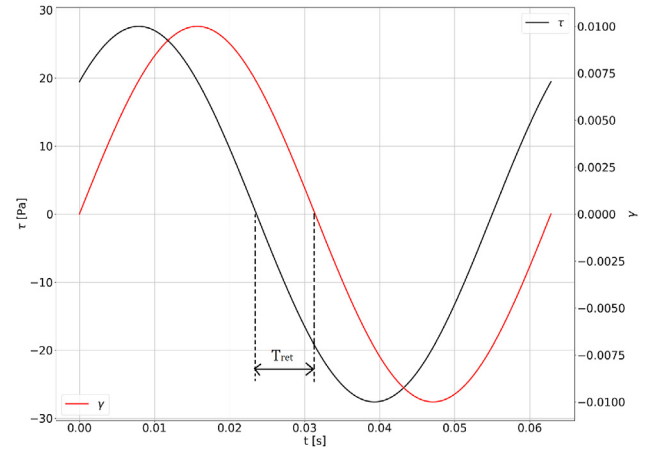

Fig. 6. Effect of viscoelasticity in the stress response of the material under oscillatory shear deformation. The parameters used are $\mu_m = \mu_k = 100$ Pa s, $k_m = 10$ kPa and $k_k = 1$ MPa. It is possible to observe the retardation time T_{ret} between stress and deformation, typical of viscoelastic behavior. It is related to the phase-lag φ through $T_{ret} = \frac{\varphi}{\omega}$, with ω the frequency of the applied oscillatory strain.

It is straightforward to observe that by integrating twice in time and taking as initial conditions $d\sigma/dt = \sigma = 0$ and $d\varepsilon/dt = \varepsilon = 0$, the elastic relation $\sigma = k_m\varepsilon$ is obtained, hence, $k_m = E_{el} = 1$ MPa. It is noteworthy that only the Maxwell spring will dictate the magnitude of the stress response, making it easier to compare with the analytical solution.

The simulation setup comprises an ordered lattice, in this case, a Simple Cubic (SC), to define a cube of constant volume $V = 0.125$ cm^3. The cube is then deformed in a periodic uniaxial compression/expansion cycle with $\varepsilon = 0.01 \sin(\omega t)$. Moreover, 4 particle sizes are simulated. Their size is computed starting from the number of particles N_{side} laying on each side of the cube such that $D + (N_{side} - 1) \cdot \delta = V^{1/3}$, leading to the values of diameters shown in Table 1. Moreover, the shear component of the contact force has been turned off. Otherwise, there would be the need to scale the shear parameters w.r.t. the normal ones (Cai et al., 2014; Collop et al., 2007; Liu et al., 2009).

As shown in Fig. 7, the solution slowly approaches a value close to the analytical solution by decreasing the particle size in a constant volume. In particular, looking at the plot of the relative percentage error, computed as,

$$\chi = 100 \left| \frac{\max(\sigma_{an}) - \max(\sigma_{sim})}{\max(\sigma_{an})} \right|, \tag{15}$$

a linear trend is observed where σ_{an} and σ_{sim} are the analytical and simulated stress response curves. This would imply that any further decrease in size would scale the error linearly, which is not ideal since computational time does not scale linearly with particle size. A better scenario would be if the error would decrease with a power of 2 or higher, such that an order of two higher accuracy justifies the increase in computational time.

Table 1
Particle size for different number of particles N in the Simple Cubic configuration of a constant volume $V = 0.125$ cm^3.

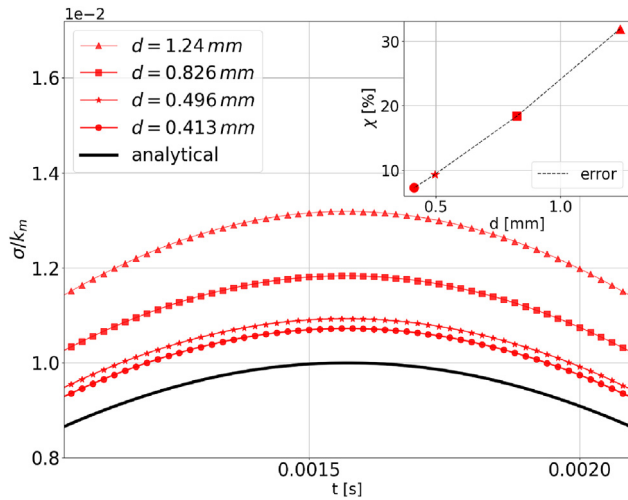| Type	N	d
Coarse	64	1.24 mm
Medium-coarse	216	0.826 mm
Medium-fine	1000	0.496 mm
Fine	1728	0.413 mm

Fig. 7. Stress output convergence of a Simple Cubic geometry under oscillatory compression at decreasing particle size and its relative error w.r.t. the analytical solution. The insert shows the relative error as a function of the particle diameter.

2.3.3. Effect of packing geometry

Remembering the simple cubic geometry of Fig. 3, where all the particles are perfectly aligned, it must be said that it is not representative of real-world applications. If one would want to observe the behavior of elastic material under uniaxial compression, for example, one is expected to see a deformation in the direction normal to the compression. However, in the case of a simple cubic, even though there is an active shear component of the contact force, no lateral deformation is obtained. Hence, the Poisson's ratio is equal to zero.

This is not true for other lattice geometries, for example in Fig. 8, where a Face Centered Cube (FCC) lattice has been used. Here, particles are displaced in the direction of compression (z-axis) and laterally (x-axis). Furthermore, using an FCC improves the accuracy of the model, as can be observed in Fig. 9. The same cyclic compression test is performed for the results of Fig. 7, with particle sizes that are slightly different due to the different lattice scaling, as shown in Table 2. In this case, the error is already much smaller in magnitude even at higher diameters, showing a non-linear regression, thus reaching more accurate solutions faster than an SC. In this case, the stress response is computed differently than for the SC (given the different configuration) and is compared again with the analytical solution to highlight the higher accuracy. The equation for the stress in an FCC is

$$\tau = \frac{\sum_{i}^{N^2} f_i}{\left(D + \sqrt{2}\left(N_{side} - 1\right) \cdot \delta\right)^2}. \tag{16}$$

If one performed the same test with an active shear Burgers element, there would be the need to scale shear contact parameters, as shown later in the manuscript, using (Potyondy & Cundall, 2004),

$$c_m^s = \frac{c_m^n}{\alpha}, \tag{17}$$

with α being the scaling coefficient. The same applies for c_k^s, y_m^s, y_k^s. Moreover, the effect of different normal-to-shear ratios has been analyzed, showing the error between the analytical solution and numerical simulation in Table 3. It is clear that a higher ratio, hence smaller shear parameters, would reduce the intensity of the total stress response. In this case, since an elastic bulk has been
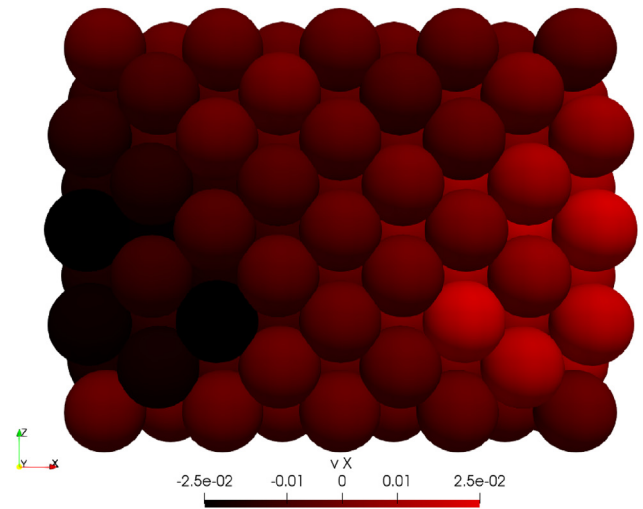

Fig. 8. Effect of uniaxial compression on the elastic Burgers material. Boundary conditions are applied similarly as for the shear oscillation case, with the only difference that here the periodic motion is substituted with a linear uniform velocity in the negative z-direction. It is clear how the particles at the sides are displacing laterally w.r.t. the direction of the applied deformation.
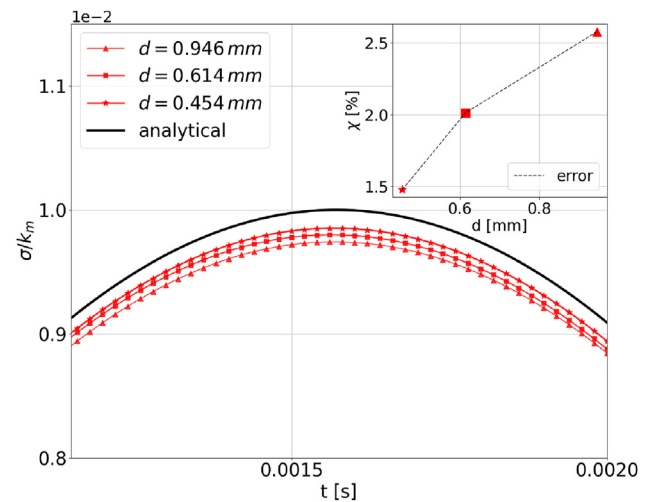

Fig. 9. Stress output convergence of a Face Centered Cube geometry under oscillatory compression at decreasing particle sizes and its relative error w.r.t. the analytical solution. Here the shear component of the force has been turned off. Differently as for the simple cubic case, here, the error does not scale linearly, showing the importance of the packing geometry/distribution for the quality of the results.

Table 2
Particle size for different number of particles N in the face-centered cube configuration of a constant volume $V = 0.125$ cm³.

Type	N	d
Coarse	172	0.946 mm
Medium	666	0.614 mm
Fine	1688	0.454 mm

simulated, hence the analytical solution is known, it would be straightforward to find the optimum ratio through a minimization algorithm, but in the case of materials in the viscoelastic regime, that change their properties depending on the time-scale of the applied stress/strain, a more detailed calibration is needed to match experimental and simulated properties as best as possible.

Table 3
Relative error between the analytical solution of an elastic body and a simulation of an elastic Burgers material when varying the normal-to-shear scaling factor α. Here, the alpha value increase has shown a corresponding relative error reduction.

α	χ
3	32.22 %
5	12.5 %
7	3.35 %
10	4.02 %

2.3.4. Accuracy of Burgers model when predicting creep behavior

To further describe the model accuracy, a creep test is used as a benchmark since the analytic solution of a Burgers material under creep is well known and it reads as follows

$$\varepsilon(t) = \sigma_0 \left[\frac{1}{k_m} + \frac{1}{k_k}\left(1 - e^{-\frac{t}{\tau_k}}\right) + \frac{t}{\mu_m} \right], \tag{18}$$

where σ_0 is a constant stress applied on the sample. The setup is the same as Sec. 2, i.e. an FCC lattice cube with the tangential component of the contact force turned off, with the difference that now we are applying constant stress on the top layer of particles in the vertical direction, not in shear, and we are measuring the relative deformation. It is like we are hanging a weight on it and looking at how much it extends w.r.t. its original length. Once again, we observed a reduction of the error at decreasing particle size, even though it is higher in magnitude when compared with the elastic behavior, as seen in Fig. 10.

3. Calibration strategy

Every time a numerical model is implemented to solve a specific mechanical system, be it a solid structure, an airflow around a wing, and so on, an error is introduced. These errors are intrinsic to the model implementation and discretization. Whenever a simulation is produced, it needs to be compared with its real-world counterpart to be sure that the variables computed in the simulation are within a relatively small margin of difference from the experimental data. Given the fact that most numerical schemes use a large set of parameters to define the model and to find the optimal parameters for a specific problem, a so-called calibration is sought
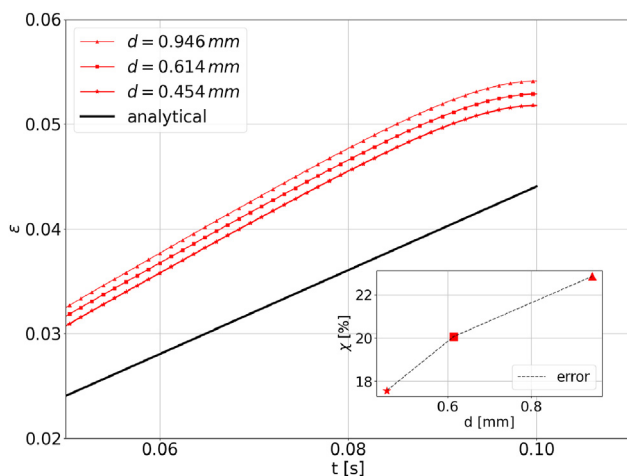

Fig. 10. Error reduction for a constant volume simulation of a creep test with decreasing particle size. The vanishing derivative at the r.h.s. of the plot is due to a low-pass filter that is applied to filter the high-frequency oscillation in the material response.

out. The calibration process is usually time-consuming, as it needs to go back and forth from simulation to error evaluation until a minimum is reached. The approach here aims to reduce the number of parameters to calibrate whilst maintaining a high-quality simulation output. Most of the work in literature dealing with the Burgers model follows a similar way of approaching this problem by finding the micro-contact parameter through the minimization of a cost function and directly inserting said parameters in the model with the proper scaling (Dondi et al., 2013; Liu et al., 2009; Majidi et al., 2016). Some work shows also the effect of fitting the normal and shear micro-parameters separately, but with the need for Oscillatory Rheometer data in both shear and compression setups (Feng et al., 2015a).

In the current study, the methodology described above will be used, which, for the Burgers model, follows these steps:

1. Rheological data from an experiment, usually in the form of the storage and loss modulus G'_{exp}, G''_{exp} is used as input in a Python script.
2. Using the following equations (Barnes, 2000), analytical values for the rheological properties as G'_{an} and G''_{an} are computed within the Python script:

$$J' = \frac{1}{k_m} + \frac{k_k}{k_k^2 + (\omega \mu_k)^2}$$

$$J'' = \frac{1}{\omega \mu_m} + \frac{\omega \mu_k}{k_k^2 + (\omega \mu_k)^2}$$

$$G'_{an} = \frac{J'}{J'^2 + J''^2} \tag{19a}$$

$$G''_{an} = \frac{J''}{J'^2 + J''2}$$

with J' and J'' being the storage and loss compliances, respectively, ω is the oscillation frequency in rad/s.

3. A cost function is defined, which evaluates the difference between the experimental and analytical data

$$f_{cost} = \sum_i^m \left[\left(\frac{G'_{an}}{G'_{exp}} - 1 \right)^2 + \left(\frac{G''_{an}}{G''_{exp}} - 1 \right)^2 \right]. \tag{19b}$$

4. The cost function is then inserted in an optimization algorithm, namely the built-in Python optimization scheme "Nelder-Mead". This algorithm minimizes the cost function by varying the model parameters μ_m, μ_k, k_m and k_k. Once the desired residuals are obtained, the optimal parameters are given and can be used as input for the DEM simulations.

Once the minimization is complete, it will return the optimal parameters, which will then be scaled as in Eq. (3) to define the micro-contact.

3.1. Limitation of Burgers model

The Burgers model has been widely used in literature to simulate the viscoelastic behavior of a wide range of materials, from asphalt(Feng et al., 2015a) to oil sands (Gbadam & Frimpong, 2017), coke/pitch mixtures (Majidi et al., 2016), to mention some. To begin with, the experimental data of Fig. 11 is taken as input for the
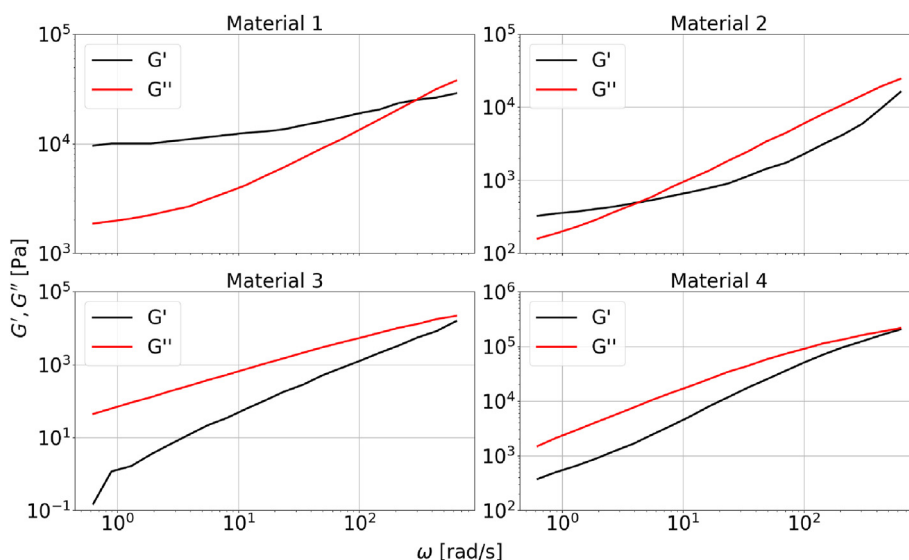
Fig. 11. Storage and loss modulus obtained from Oscillatory Shear Rheometer experiments of different viscoelastic materials. This is the dataset used as a base for the calibration as each material shows a noticeably different viscoelastic behavior on a wide range of frequency, hence testing the ability of the model to describe a large class of materials.

calibration. This dataset is of particular relevance as not only it shows a variety of materials behavior, but it also covers a wide range of applications, with an angular frequency spanning from 0.63 rad/s to 632 rad/s. If one would try to use the fitting procedure described in Sec. 3, let's say on material 1 of Fig. 11, for example, one would obtain something similar to the plot of Fig. 12. This is mainly due to the lack of parameters to properly fit through a large dataset (Mazurek & Iwaski, 2017). Moreover, the quality of the fitting has been quantified by computing the root mean square deviation as

$$RMSD = \frac{100}{\max(y) - \min(y)} \sqrt{\frac{\sum_i^N (\bar{y}_i - y_i)^2}{N}}, \qquad (20)$$

where $\bar{y}$ is the predicted value, in this case, the simulation output, and y is the real value, with N being the number of data points.

One way to overcome this issue is to reduce the range on which the data is fitted, similarly to what Feng et al. (Feng et al., 2015b, pp. 423–433) proposed, and then perform the normal calibration procedure on each data chunk separately before rejoining the data
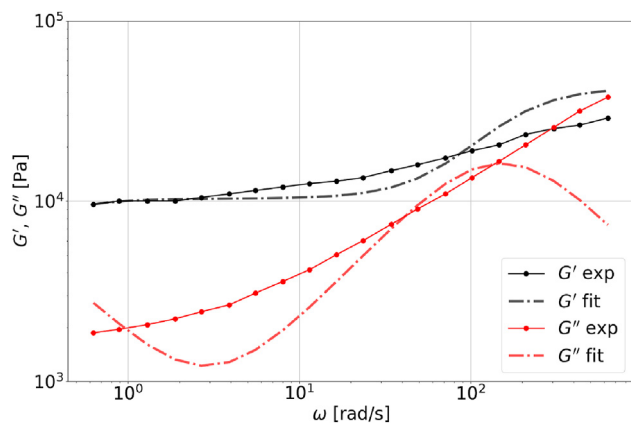
together. In particular, 5 chunks have been chosen in our study, each composed of 4 frequencies, which lead to the calibrated parameters found in Table 4. Even though this works quite nicely for the fitting procedure, as shown in Fig. 13, it leads to some problems, especially when going into the simulation realm. The biggest drawback is that a non-constant set of parameters is produced for each chunk and not only do they differ greatly, as it can be seen in Table 4, hence making the use of an average not feasible, but it also limits the use of this model in an industrial process simulation since there would be the need to adapt parameters to the local shear rate.

Once the parameters are known, it is possible to perform the frequency sweep simulation of the Oscillatory Shear Rheometer.

As shown in Fig. 14, in addition to a non-constant set of parameters, the error is not acceptable to consider this model accurate enough, at least not on a large dataset. Moreover, some notes are needed about this result. First, the amplified frequency method (Liu & You, 2011) has been used to improve the speed of the low-frequency simulations, multiplying the damping coefficients and the frequency by a constant value. Even though Liu et al. (Liu & You, 2011) used this method specifically for asphalt mixtures simulations with the Burgers model, it proved to be applicable for a more general case as well. Secondly, the ratio between normal and shear parameters has been chosen to be $\alpha = 2.7$, which worked well for material 1 but not for other materials of the same dataset, meaning a proper calibration of this parameter is needed. Overall, given the limits of Burgers material to fit through the data with a unique set of parameters, which would highly compromise the applicability in

Fig. 12. Attempt of fitting the experimental data of material 1 using the Burgers model. Given the limited number of relaxation times of the model, it is heavily limited in accurately fitting through a wide range of frequencies, giving an RMSD of 40% for G' and 35 % for G".

Table 4
Calibrated parameters of Burgers model relative to material 1. The dataset has been divided into subsets with a smaller range of frequencies to obtain a good quality fit of the experimental output. To notice how certain parameters vary by some order of magnitude at increasing frequency. Damping coefficients μ_m and μ_k are in [Pa·s], and spring coefficients k_m and k_k are in [Pa].

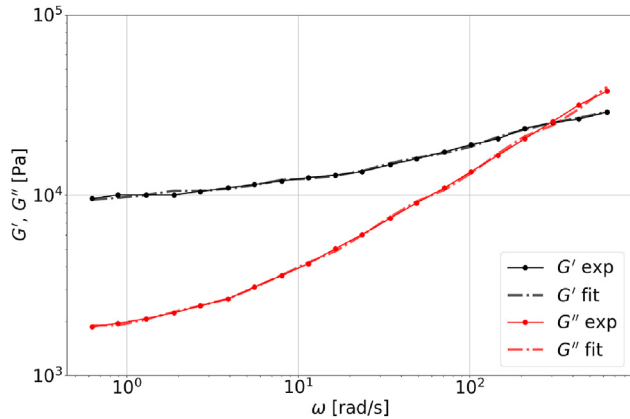| ω range [rad/s]	μ_m	μ_k	k_m	k_k
0.6–1.9	$1.325 \cdot 10^5$	$1.55 \cdot 10^4$	$1.36 \cdot 10^4$	$3.24 \cdot 10^4$
2.7–8.1	$3.76 \cdot 10^4$	$0.31 \cdot 10^4$	$1.8 \cdot 10^4$	$2.62 \cdot 10^4$
11.5–34.1	$0.85 \cdot 10^4$	658.1	$3.22 \cdot 10^4$	$2.14 \cdot 10^4$
48.8–146.5	$0.16 \cdot 10^4$	220.2	$7.33 \cdot 10^4$	$2.56 \cdot 10^4$
209.3–632.4	$3.75 \cdot 10^2$	77.86	$5.03 \cdot 10^5$	$3.98 \cdot 10^4$

Fig. 13. Improved fitting of experimental data of material 1 when using the Burgers model. This result is obtained by dividing the dataset into smaller subsets and performing the analytical fitting on the latter. The fit quality is noticeably increased, giving an RMSD of 1–2% for the whole dataset. However, it produced non-constant parameters through the frequency range.

industrial processes, the decision to implement a Generalized Maxwell model has been taken.

3.2. Fitting quality of a generalized Maxwell model

When performing the analytical fitting of experimental data with the generalized Maxwell model, the same procedure as the one described in Sec. 3 for the Burgers constitutive relation is followed, with the difference that the equations used to compute the predicted storage and loss moduli are respectively (Barnes, 2000)

$$G' = \sum_{j}^{4} \frac{k_j(\omega\tau_j)^2}{1+(\omega\tau_j)^2} + k_e, \quad G'' = \sum_{j}^{4} \frac{\omega\mu_j}{1+(\omega\tau_j)^2}. \quad (21)$$

Before diving into the 4-element model, it is noteworthy to mention that a 3-element model has been previously used to fit the experimental data with poor results, Fig. 15, giving values of $RMSD_{G'} = 19\%$ and $RMSD_{G''} = 8\%$, which is an improvement w.r.t. the Burgers model, but is not enough, hence the choice for a 4-element approach. The optimization algorithm is done in Python,
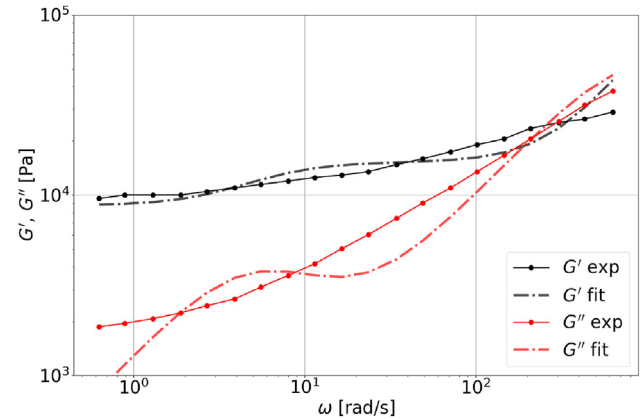

Fig. 14. Simulation output with fitted Burgers model parameters of oscillatory shear deformation for material 1. The parameters used for the simulation are shown in Table 4, hence with non-constant parameters throughout the dataset. The RMSD for G' is 25%, while for G" is 21%.

Fig. 15. Analytical fitting of experimental data of material 1 using the generalized Maxwell model constitutive relation with 3 elements and a spring. The combination of a large dataset and 3 timescales is not enough to achieve a good fit.
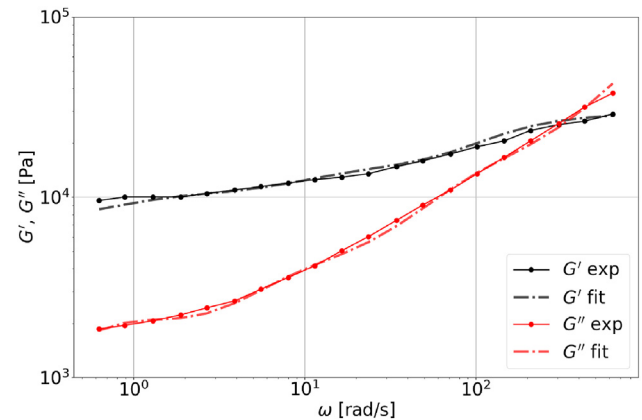

Fig. 16. Analytical fitting of experimental data of material 1 using the generalized Maxwell model constitutive relation with 4 elements and a spring. It is immediate to observe a good quality fitting through all the points, which gives 4% RMSD for G' and 3% for G" while keeping the parameters constant. This is achieved thanks to the larger number of relaxation times of the generalized Maxwell model.

leading to the fit of Fig. 16 for material 1 of the dataset of Fig. 11, the same fit quality is achieved in the other materials of Fig. 11 as well, not shown for simplicity. Moreover, the calibrated parameters for each material are shown in Table 5 and the relative RMSD errors of each material fit in Table 6.

3.3. Calibrating the normal-to-shear scaling parameter

As already discussed in Sec. 3.1, while the use of Eq. (17) is largely used in literature to address the scaling between normal and shear micro-contact parameters(Cai et al., 2014; Potyondy & Cundall, 2004; Yu & Shen, 2012), in this study it has been decided to improve accuracy by tuning α for each material in the experimental dataset. This is done by executing a calibration algorithm in a more classical way, i.e. by simulating a frequency sweep with a first guess value, evaluating the error w.r.t. the experimental data, updating the value, and re-running the frequency sweep until a minimum is reached. The value update is done separately in a Python script using a scalar minimization algorithm, namely the Bounded Brent method. Moreover, given the fact that the low-frequency simulations can not be amplified in this case, as the method used in (Liu & You, 2011) has been
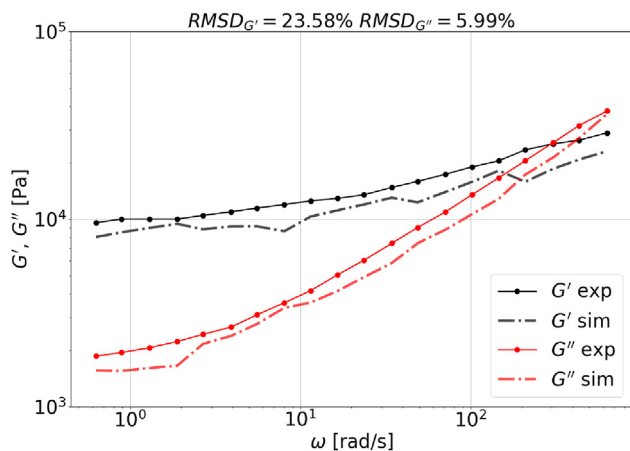
Table 5
Calibrated macro parameters of the generalized Maxwell model for the experimental data shown in Fig. 11. Note how the parameters stay constant for each material, unlike the Burgers model case. The need for increased relaxation times, hence more parameters, is justified. Damping coefficients $\mu_{1,2,3,4}$ are in [Pa·s] and spring coefficients $k_{1,2,3,4,e}$ are in [Pa].

Material	μ_1	μ_2	μ_3	μ_4	k_1	k_2	k_3	k_4	k_e
1	3711	108.7	63.1	373.4	3067	$1.39 \cdot 10^4$	$3.98 \cdot 10^6$	4065	7423
2	24.6	251.2	49.4	50.7	1698	160	337.4	$5.88 \cdot 10^4$	232
3	46.1	14.5	7.3	4.8	$4.78 \cdot 10^4$	1609	116.1	$9.92 \cdot 10^4$	0
4	535.2	0	927.4	681.4	$4.52 \cdot 10^5$	0	$6.73 \cdot 10^4$	3785	359.4

Table 6
Root mean square deviations of the analytical fit of the experimental data shown in Fig. 11.

Material	$RMSD_{G'}$	$RMSD_{G''}$
1	4.16%	3.27%
2	1.21%	1%
3	1.49%	0.57%
4	3.43%	2%

proven to work with Burgers but not with other models, it has been decided to perform the calibration in the range of frequency $\omega > 100$ rad/s, and then run only one frequency sweep at the lower frequencies with the calibrated value of α to check if the simulation accuracy is maintained. Starting from a first guess value of $\alpha = 1$, the root mean square deviation, Eq. (20), is checked at each iteration, and the threshold to trigger calibration is $\max(RMSD_{G'}, RMSD_{G''}) \geq 10\%$. To be noted that a smaller value for the threshold can be used, depending on the specific application. Here, given the informatory and descriptive purpose of the manuscript, a value of 10% is used. Once the calibration procedure is completed, it gives the optimal values of α of Table 7.

The contact parameters and the normal-to-shear ratio are now calibrated for each material. Hence it is possible to check the quality of the simulations at lower frequencies by running a single frequency sweep in the range $\omega > 10$ rad/s. A Face Centered Cube packing is used with N = 666 particles with diameter $D = 0.4$ mm and a deformation $\gamma = 0.01$ is applied, the oscillation amplitude is $A = 0.01H$, with H being the height of the cube. The aforementioned simulations produced the plots of Fig. 17 comparing the simulation output against its experimental counterpart. It can be immediately seen how the error is reduced w.r.t. the Burgers model case, as highlighted by Table 8, both for G' and G'', even though the frequency range is smaller. Moreover, it must be remembered that the parameters are constant throughout the dataset, as opposed to the Burgers model case. Notably, all materials in the study, except material 1, produced a scaling factor $\alpha \approx 1$. It is not a case that material 1 is also the only one with $G' > G''$, whereas the opposite is observed for the other cases. This can be explained by the fact that a more elastic material's shear interactions are overestimated. At the same time, they have the same or even higher magnitude in more viscous materials, as expected. To conclude, not all materials managed to stay below the 10% limit error.

Table 7
Normal to shear ratio calibrated parameters for the materials of the experimental dataset. Only material 1 has a ratio significantly larger than one, being also the only material with $G' > G''$ in the whole frequency range of interest.

	Material 1	Material 2	Material 3	Material 4
α	2.135	1.089	1.026	1.017

4. Oscillatory plate-plate shear rheometer simulation

The results obtained with the cube simulations are promising but limited since they represent an ideal case with geometrical symmetry, which is far from real-world cases. For a more meaningful comparison, it has been decided to simulate the behavior of materials 1 and 2 in a plate-plate shear rheometer. It comprises a fixed plate on the bottom and a mechanical drive plate on the top. In between, the material is placed. Once the setup is complete, the top plate rotates around its axis with a strain-controlled motion, i.e. the oscillations follow a function of the type $\theta_0 \sin(\omega t)$, where θ_0 is the amplitude of oscillation angle, given by $\theta_0 = \frac{180\gamma H}{\pi D}$. The value of $\gamma = s/h$ is chosen as the shear deformation at a distance $D/2$ from the center, where D is the plate diameter, s is the arc length at $D/2$, and H is the distance of the plates, Fig. 18. Moreover, as done for the cube, a frequency sweep is carried out in the same range.

To reduce the number of particles, instead of simulating the full disk, a ring is created with the following geometry: internal diameter $D_{int} = 0.01$ m, external diameter $D_{ext} = 0.012$ m, plate-plate distance $H = 10^{-3}$ m, particle diameter $D = 10^{-4}$ m, and deformation angle $\theta = 0.0955°$. This angle is calculated starting from a deformation $\gamma = 0.01$ at the external radius, Fig. 19. The geometrical parameters are not representative of a real setup. Still, they are chosen according to particle size to maintain good accuracy, following the convergence study of the previous sections.

An oscillatory motion is applied on the top layer of particles, with the same frequency range used on the cube. The stress is computed as the sum of the forces in the tangential direction on every single particle, given by

$$\sigma = \frac{\sum_i^N f_{i,\theta}}{A_{ring}} \tag{22}$$

where $f_{i,\theta} = f_{i,y}\cos\left(atan2\left(\frac{y_i}{x_i}\right)\right) - f_{i,x}\sin\left(atan2\left(\frac{y_i}{x_i}\right)\right)$ is the ith particle tangential force, with $f_{i,x}, f_{i,y}$ its x and y force components and x_i, y_i its x and y coordinates. Regarding the deformation, in a plate-plate geometry the value of γ changes linearly in the radial direction. To account for this, an average deformation is considered as $\hat{\gamma} = \frac{\gamma_{ext} + \gamma_{int}}{2} = 0.00916$. Applying the data analysis described in Sec. 2.3 to the stress output and using the calibrated parameters for material 1 and material 2, the plot of Figs. 20 and 21 are obtained. The model shows how, even in more complex systems, it can predict the rheology of a given material once the parameters have been calibrated for a given range of frequencies. While for material 1 the errors are both in line with what was obtained in the cube system, with $RMSD_{G'} = 14.5\%$ and $RMSD_{G''} = 11.43\%$, a different outcome is observed for material 2, where the error for G' is $RMSD_{G'} = 6.8\%$. At the same time, it is quite high for G'', giving $RMSD_{G''} = 21.4\%$, especially due to the high-frequency results. In general, the model can behave according to the
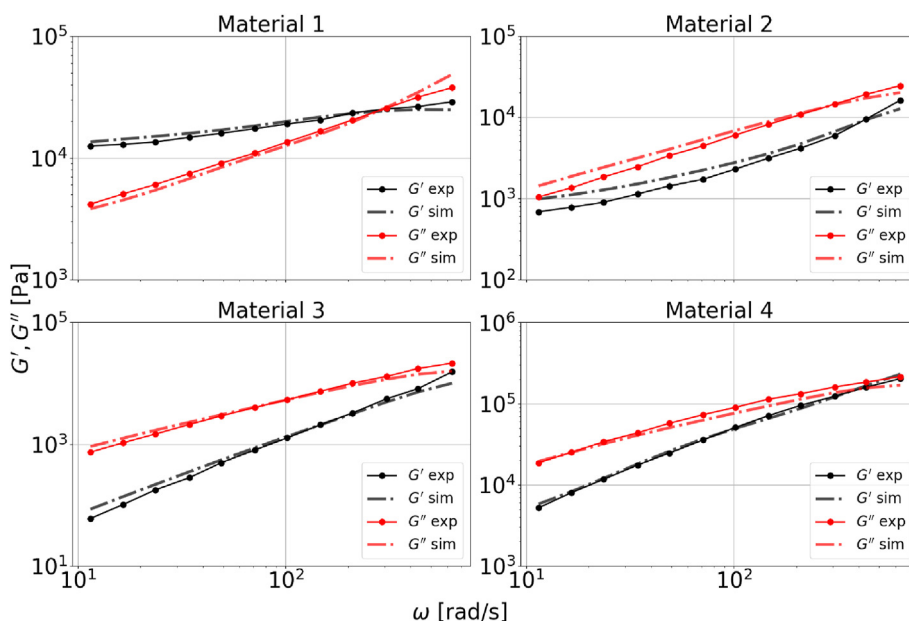
Fig. 17. Simulation output of the frequency sweep oscillatory shear deformation performed on the materials of Fig. 11, with calibrated macro parameters from Table 5 and normal to shear ratio from Table 7. Quantitatively, the rheological properties are predicted with good accuracy overall. Some inaccuracies are present qualitatively, for example regarding material 4, where the characteristic frequency at which G' and G'' overlap is highly underestimated. On the other hand, a good prediction is obtained for material 1 regarding the same quantity.

Table 8
Root mean square deviation, shown as relative percentage error, of the simulation output vs the experimental data.

	Material 1	Material 2	Material 3	Material 4
$RMSD_{G'}$	9.65 %	7.01 %	10.39 %	4.38 %
$RMSD_{G''}$	9.82 %	6.36 %	9.43 %	9.94 %

rheological properties of the calibrated material in simple and more complex systems but with reduced accuracy. It might be due to the numerical errors that arise with randomness and the increased complexity of internal structures. However, this is not clear, and it needs to be investigated further.
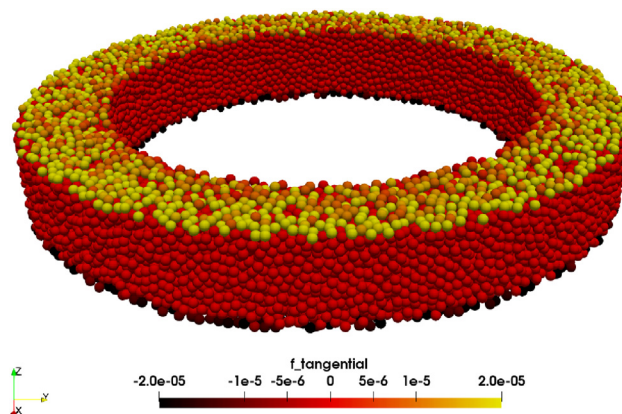

Fig. 19. Graphical representation of the ring shear rheometer simulation. The applied motion on the top layer of particles can be noted, given by a radial gradient of the tangential force. These are the same particles used to compute the stress as the sum of the forces on every single particle in the tangential direction, divided by the ring area.
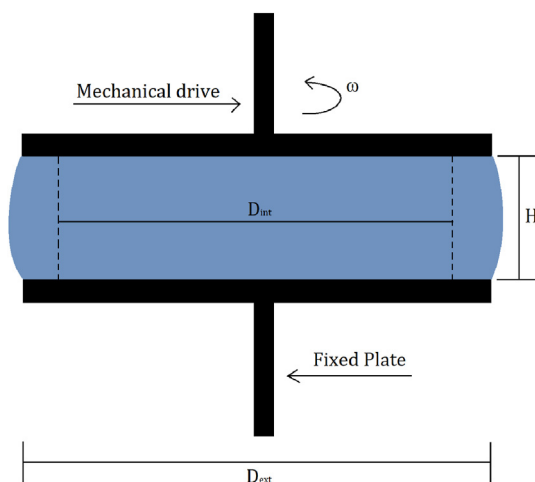

Fig. 18. Simple geometrical representation of plate-plate shear rheometer. In experiments, the material in between is not constrained laterally. Hence it deforms due to centrifugal inertia. This is a limitation in experiments as higher frequencies/amplitudes lead to an overflow of the sample from the setup. The simulation is based on this configuration, but it is not a digital twin of an existing setup.
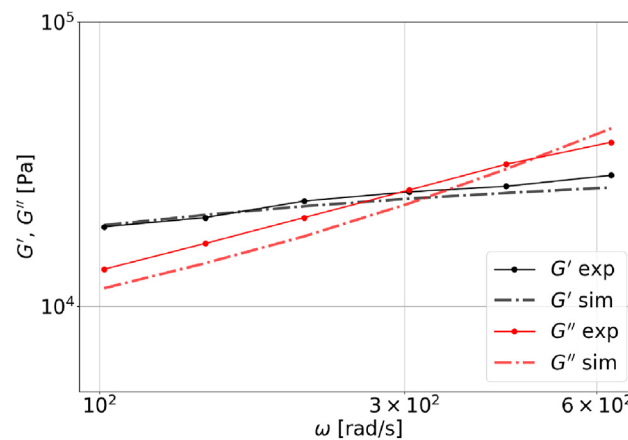

Fig. 20. Comparison of the simulation output from the ring shear rheometer tests and the experimental dataset used to calibrate material 1. The accuracy w.r.t. the cube case is only slightly decreased, and the model can predict the material's rheological properties.
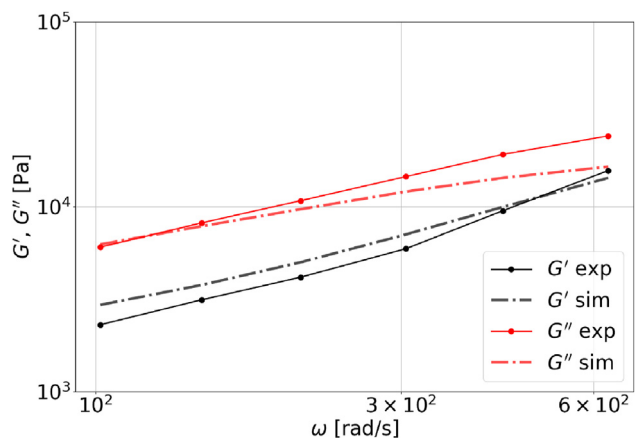
Fig. 21. Comparison of the simulation output from the ring shear rheometer tests and the experimental dataset used to calibrate material 2. In this case, the accuracy for the storage modulus is still maintained relatively low, while a larger divergence is observed at the higher frequency values.

5. Conclusions

The way the model is implemented, especially due to the presence of the bond, makes it prone to disturbances in the stress response arising from the influence of the system eigenfrequencies, which are more prominent than in the experiments due to the higher inertia of the measurement instruments. Moreover, the fact that an ordered lattice is used to simulate oscillatory rheometer tests increases the magnitude of such an effect, leading to secondary oscillations in the stress response amplitude. The use of the Fast Fourier Transform solves this issue, but not entirely, as the stress response amplitude highly depends on the particles size and lattice configuration; in other words, the mass matrix of the system is a key factor in the quality of the stress response, and an ordered lattice would increase the values on the diagonal, hence amplifying the eigenfrequency effect. This effect can be slightly countered with smaller particles, thus with lower inertia that would reduce the eigenfrequencies oscillations. Furthermore, a Burgers model has been chosen to impose the viscoelastic interaction between particles. The choice for this model resides in the fact that it has already been extensively implemented in literature, mostly for asphalt and bituminous materials (Cai et al., 2014; Collop et al., 2007; Dondi et al., 2013; Feng et al., 2015a; Wang et al., 2020; Yu & Shen, 2012). Moreover, since the focus of our present contribution is to obtain a model able to characterize any viscoelastic material, an experimental dataset is used, which does not comprise bitumen and/or asphalt in such a way as to test the limit of the model. The calibration is done analytically, fitting the experimental data with the Burgers model and substituting the optimal macro-parameters in the constitutive micro-contact relation after appropriate scaling. During this phase, it has been observed that the Burgers model cannot properly fit on a large dataset. Hence, the experimental data is divided into subsets, and fitting is performed on every subset. After comparing the simulation data with the experimental dataset, it has been shown that the Burgers model is not suited for any material and lacks precision when dealing with a large dataset due to its low number of parameters.

Keeping in mind the goal of the article, which is to be able to obtain a model that maintains accuracy regardless of the size of the dataset or the material needed to be characterized, a new model with a larger number of parameters, hence more relaxation times, is implemented, namely the Generalized Maxwell model. This model immediately shows good precision when fitting the experimental data without dividing the data into subsets to maintain a good quality, hence obtaining a unique set of parameters for each material. Moreover, the model's accuracy in a more complex system has been studied, showing how the accuracy is maintained for some materials while it partially reduces for other materials, especially in the higher frequency domain.

Ultimately, this model aims at reducing the complexity of simulating processes involving viscoelastic materials using mesh-based methods. The main advantage is the meshless nature of the presented model, resulting in easier and faster modeling of the computational domain. This is of interest when dealing with moving boundaries, which are challenging to use in a mesh-based model. The use of discrete particles makes it easier to capture wall-material interactions in a more natural way, together with material flows. Future extensions of our present work could include bond breakage and particle-wall contacts and predict the non-linear behavior of real materials. In this way, it would be possible to simulate large-scale industrial processes involving viscoelastic materials and optimize those processes to reduce energy consumption, product quality, or yield.

Declaration of interests

The authors declare that they have no known competing financial interests or personal relationships that could have appeared to influence the work reported in this article.

Appendix A. Supplementary data

Supplementary data to this article can be found online at https://doi.org/10.1016/j.partic.2023.11.001.

References

Barnes, H. A. (2000). *A Handbook of elementary rheology*. Institute of Non-Newtonian Fluid Mechanics, University of Wales.

Bottoni, M., Mazzotti, C., & Savoia, M. (2007). A finite element model for linear viscoelastic behaviour of pultruded thin-wall beams under general loadings. *International Journal of Solid and Structures, 45*, 770–793. https://doi.org/10.1016/j.ijsolstr.2007.08.028

Cai, W., McDowell, G., & Airey, G. (2014). Discrete element visco-elastic modelling of a realistic graded asphalt mixture. *Soils and Foundations, 54*, 12–22. https://doi.org/10.1016/j.sandf.2013.12.002

Cao, W. (2020). General fractional models for linear viscoelastic characterization of asphalt cements. *Journal of Rheology, 64*, 1439–1453. https://doi.org/10.1122/8.0000096

Collop, A. C., McDowell, G. R., & Lee, Y. (2007). On the use of discrete element modelling to simulate the viscoelastic deformation behaviour of an idealized asphalt mixture. *Geomechanics and Geoengineering: An International Journal, 2*, 77–86. https://doi.org/10.1080/17486020701243128

Cundall, P. A., & Strack, O. D. L. (1979). A discrete numerical modelling for granular assemblies. *Géotechnique, 29*, 1.

Dondi, G., Vignali, V., Pettinari, M., Mazzotta, F., Simone, A., & Sangiorgi, C. (2013). Modeling the dsr complex shear modulus of asphalt binder using 3d discrete element approach. *Construction and Building Materials, 54*, 236–246. https://doi.org/10.1016/j.conbuildmat.2013.12.005

Favero, J., Secchi, A., Cardozo, N., & Jasak, H. (2010). Viscoelastic flow analysis using the software openfoam and differential constitutive equations. *Journal of Non-newtonian Fluid Mechanics, 165*, 1625–1636. https://doi.org/10.1016/j.jnnfm.2010.08.010

Feng, H., Pettinari, M., & Stang, H. (2015a). Study of normal and shear material properties for viscoelastic model of asphalt mixture by discrete element method. *Construction and Building Materials, 98*, 366–375. https://doi.org/10.1016/j.conbuildmat.2015.08.116

Feng, H., Pettinari, M., & Stang, H. (2015b). *8th rilem international symposium on testing and characterization of sustainable and innovative bituminous materials* (pp. 423–433). RILEM, Elsevier.

Gbadam, E. K. (2017). *Characterization and numerical simulation of the microstructural and micromechanical viscoelastic behavior of oil sands using the discrete element method*. Ph.D. thesis, Missouri University of Science and Technology.

Gbadam, E., & Frimpong, S. (2017). Micromechanical and microstructural dem modeling of the viscoelastic behavior of oil sands. *Advanced Materials Science, 2*, 1–11. https://doi.org/10.15761/AMS.1000116

Giesekus, H. (1982). A simple constitutive equation for polymer fluids based on the concept of deformation-dependent tensorial mobility. *Journal of Non-newtonian Fluid Mechanics, 11, 69–109.*

Katouzian, M., Vlase, S., & Scutaru, M. L. (2021). Finite element method-based simulation creep behaviour of viscoelastic carbon-fiber composite. *MDPI polymers, 13*. https://doi.org/10.3390/polym13071017

Liu, Y., Dai, Q., & You, Z. (2009). Viscoelastic model for discrete element simulation of asphalt mixtures. *Engineering Mechanics, 135*. https://doi.org/10.1061/(ASCE)0733-9399(2009), 135:4(324).

Liu, Y., & You, Z. (2011). Determining burger's model parameters of asphalt materials using creep-recovery testing data. *Journal of Engineering Mechanics, 137*, 355–365. https://doi.org/10.1061/41008(334)3

Majidi, B., Taghavi, S. M., Fafard, M., Ziegler, D. P., & Alamdari, H. (2016). Discrete element method modeling of the rheological properties of coke/pitch mixtures. *MDPI - Materials, 9*. https://doi.org/10.3390/ma9050334

Mazurek, G., & Iwaski, M. (2017). Modelling of asphalt concrete stiffness in the linear viscoelastic region. *IOP Conference Series: Materials Science and Engineering, 245*.

Mohammed, M. A. P., Tarleton, E., Charalambides, M. N., & Williams, J. G. (2013). Mechanical characterization and micromechanical modeling of bread dough. *Journal of Rheology, 57*, 249–272. https://doi.org/10.1122/1.4768463

Potyondy, D. O., & Cundall, P. A. (2004). A bonded particle model for rocks. *International Journal of Rock Mechanics and Mining Sciences, 41*, 1329–1364. https://doi.org/10.1016/j.ijrmms.2004.09.011

Ren, J., & Sun, L. (2016). Generalized maxwell viscoelastic contact model-based discrete element method for characterizing low-temperature properties of asphalt concrete. *Journal of Materials in Civil Engineering, 28*. https://doi.org/10.1061/(ASCE)MT.1943-5533.0001390

Tsai, W., & Miller, G. H. (2014). Numerical simulations of viscoelastic flow in complex geometries using a multi-mode giesekus model. *Journal of Non-newtonian Fluid Mechanics, 210*, 29–40. https://doi.org/10.1016/j.jnnfm.2014.05.002

Wang, Y., & Alonso-Marroquin, F. (2009). A finite deformation method for discrete modelling: Particle rotation and parameter calibration. *Granular Matter, 11*, 331–343. https://doi.org/10.1007/s10035-009-0146-2

Wang, H., Behnia, B., Buttlar, W. G., & Reis, H. (2020). Development of two-dimensional micromechanical, viscoelastic and heterogeneous-based models for the study of block cracking in asphalt pavements. *Construction and Building Materials, 244*. https://doi.org/10.1016/j.conbuildmat.2020.118146

Yu, H., & Shen, S. (2012). A micromechanical based three-dimensional dem approach to characterize the complex modulus of asphalt mixtures. *Construction and Building Materials, 38*, 1089–1096.

Zubov, A., Wilson, J. F., Kroupa, M., Soos, M., & Kosek, J. (2019). Numerical modeling of viscoelasticity in particle suspensions using the discrete element method. *Langmuir, 35*, 12754–12764. https://doi.org/10.1021/acs.langmuir.9b01107